Parameterization of the Spatial Variability of Rain for Large-Scale Models and Remote Sensing

Z. J. LEBO*

Cooperative Institute for Research in Environmental Sciences, University of Colorado Boulder, and Chemical Sciences Division, NOAA/Earth System Research Laboratory, Boulder, Colorado

C. R. WILLIAMS

Cooperative Institute for Research in Environmental Sciences, University of Colorado Boulder, and Physical Sciences Division, NOAA/Earth System Research Laboratory, Boulder, Colorado

G. FEINGOLD

Chemical Sciences Division, NOAA/Earth System Research Laboratory, Boulder, Colorado

V. E. LARSON

Department of Mathematical Sciences, University of Wisconsin–Milwaukee, Milwaukee, Wisconsin

(Manuscript received 4 March 2015, in final form 1 July 2015)

ABSTRACT

The spatial variability of rain rate R is evaluated by using both radar observations and cloud-resolving model output, focusing on the Tropical Warm Pool–International Cloud Experiment (TWP-ICE) period. In general, the model-predicted rain-rate probability distributions agree well with those estimated from the radar data across a wide range of spatial scales. The spatial variability in R, which is defined according to the standard deviation of R (for R greater than a predefined threshold $R_{\min}$) $\sigma(R)$, is found to vary according to both the average of R over a given footprint $\mu(R)$ and the footprint size or averaging scale Δ. There is good agreement between area-averaged model output and radar data at a height of 2.5 km. The model output at the surface is used to construct a scale-dependent parameterization of $\sigma(R)$ as a function of $\mu(R)$ and Δ that can be readily implemented into large-scale numerical models. The variability in both the rainwater mixing ratio q_r and R as a function of height is also explored. From the statistical analysis, a scale- and height-dependent formulation for the spatial variability of both q_r and R is provided for the analyzed tropical scenario. Last, it is shown how this parameterization can be used to assist in constraining parameters that are often used to describe the surface rain-rate distribution.

1. Introduction

Although the spatial resolution of general circulation models (GCMs) has continued to increase, many state-of-the art models lack a physical representation of cloud and/or rain spatial variability and continue to represent convective and stratiform cloud processes using distinctly different formulations. To resolve convective processes, a grid spacing of less than 4 km is necessary (e.g., Weisman et al. 1997), whereas resolving shallow warm clouds requires orders-of-magnitude smaller grid spacings. The GCMs used in the most recent Intergovernmental Panel on Climate Change (IPCC) report have grid spacings exceeding those needed to resolve convection by more than an order of magnitude (IPCC 2007). Therefore, in such large-scale models, representing the spatial heterogeneity of cloud and precipitation characteristics remains a subgrid-scale process. Moreover, the use of different frameworks to represent stratiform and convective clouds results in a somewhat arbitrary

* Current affiliation: Department of Atmospheric Science, University of Wyoming, Laramie, Wyoming.

Corresponding author address: Z. J. Lebo, Dept. of Atmospheric Science, University of Wyoming, 1000 East University Ave., Laramie, WY 82071.
E-mail: zlebo@uwyo.edu

DOI: 10.1175/JAMC-D-15-0066.1

distinction between cloud types; in nature, there is a continuum between these cloud types.

Recent advances in the representation of subgrid-scale processes in climate models, for example, the Cloud Layers Unified by Binomials (CLUBB) parameterization (Golaz et al. 2002; Larson and Golaz 2005; Larson et al. 2012; Larson and Griffin 2013; Griffin and Larson 2013) or the parameterizations of Cheng and Xu (2009) and Boutle et al. (2014), use a unified framework that can represent clouds and precipitation across various scales and regimes. Such parameterizations are inherently designed to be used at grid spacings that exceed those typically used for resolving convective processes. These frameworks form the basis of the representation of subgrid-scale processes. Knowing the spatial variability of a particular field can assist in constructing a spatial distribution of that field, but for some fields, for example, rain rate and rain mixing ratio, the relationship between the spatial variability and resolved quantities remains unknown. The CLUBB parameterization relies on an assumed relationship between the mean rainwater mixing ratio $\mu(q_r)$ and the standard deviation of the rainwater mixing ratio $\sigma(q_r)$ within raining regions (e.g., Larson and Griffin 2013; Griffin and Larson 2013). Moreover, a similar relationship between the mean rain rate $\mu(R)$ and the standard deviation of the rain rate $\sigma(R)$ is also of interest, specifically for diagnosing the accumulated surface precipitation. Spatial means and standard deviations are the focus of this work (unless otherwise noted). Part of the goal of this work is to look for a predictable dependence of $\sigma(R)$ on $\mu(R)$ and $\sigma(q_r)$ on $\mu(q_r)$, and if so, to determine functional forms for $\sigma(R)$ and $\sigma(q_r)$ using well-resolved quantities.

The tropics are the focus of this study (although results are presented in the appendix for a continental convection case to illustrate the potential generality of the results presented herein). This region is selected because of the availability of high-quality radar data from the Tropical Warm Pool–International Cloud Experiment (TWP-ICE).

Furthermore, there are a few motivations for constraining $\sigma/\mu(R)$ and $\sigma/\mu(q_r)$. 1) Understanding the small-scale variability of R and q_r is important because many rain processes are highly nonlinear. 2) Unified parameterizations may benefit from a functional form to represent subgrid-scale variability in R and q_r because prognosing $\sigma(R)$ and $\sigma(q_r)$ is both complicated and computationally expensive. 3) GCMs tend to overpredict the amount of light precipitation (i.e., $<20\,\text{mm day}^{-1}$) (e.g., Dai and Trenberth 2004; Dai 2006; Stephens et al. 2010), which has been attributed to deep and shallow convective precipitation, especially in the tropics (e.g., Stephens et al. 2010). A bias in surface precipitation can have important feedbacks on subsequent cloud formation and evaporative cooling. Moreover, verpredicting light precipitation can result in a low bias in $\sigma(R)$. 4) Understanding subgrid-scale variability in rain rates and mixing ratios is also important for satellite-retrieved measurements (e.g., Meneghini and Jones 1993), in which beamfilling parameterizations are often necessary to accurately represent subpixel-scale variability (e.g., Yang et al. 2006; Turk et al. 2008; Sapiano and Arkin 2009; Wolff and Fisher 2009).

The remainder of the paper is organized as follows. Section 2 describes the radar data and model simulation. Section 3 discusses the analysis of the radar data and the model output in the context of determining a useful and robust functional form for $\sigma(R)$. Based on the model output, section 4 presents an analysis of the spatial variability in q_r and R as a function of height. This section concludes with a scale- and height-dependent parameterization of the variability in surface rain rate and rainwater mixing ratio. Section 5 reviews the main results of this study and discusses the potential applications of the findings herein. The appendix discusses an additional simulation of a continental squall line in the context of the results found for tropical convection.

2. Methods

a. CPOL radar data

The Australian Bureau of Meteorology (BoM) operates a C-band (5.6 GHz) polarimetric scanning radar (CPOL) near Darwin in the Northern Territory of Australia (Keenan et al. 1998). The CPOL radar is a real-time operational radar with a fixed 10-min scan strategy that collects data from 16 conical sweeps at elevation angles from 0.5° to 42°. It operated continuously during TWP-ICE and included the 18–26 January 2006 period, providing rain-rate estimates every 10 min for a total of 1296 radar scans. By alternating between horizontal and vertical transmit polarizations, the CPOL radar measures reflectivity in two polarizations (Z_h and Z_v) to estimate differential reflectivity Z_{dr} (Kumar et al. 2013). Radial measurements of Z_h and Z_{dr} are collected at 250-m range resolution and then resampled to a Cartesian grid with 2.5 km × 2.5 km horizontal and 0.5-km vertical resolutions (May and Keenan 2005). Using three-dimensional linear interpolation, the NCAR-supported Sorted Position Radar Interpolation (SPRINT) software is used to convert constant-altitude plan position indicator (CAPPI) observations onto the 2.5 km × 2.5 km horizontal grid (Kumar et al. 2013). The eight nearest neighbors in azimuth, elevation, and range are used in

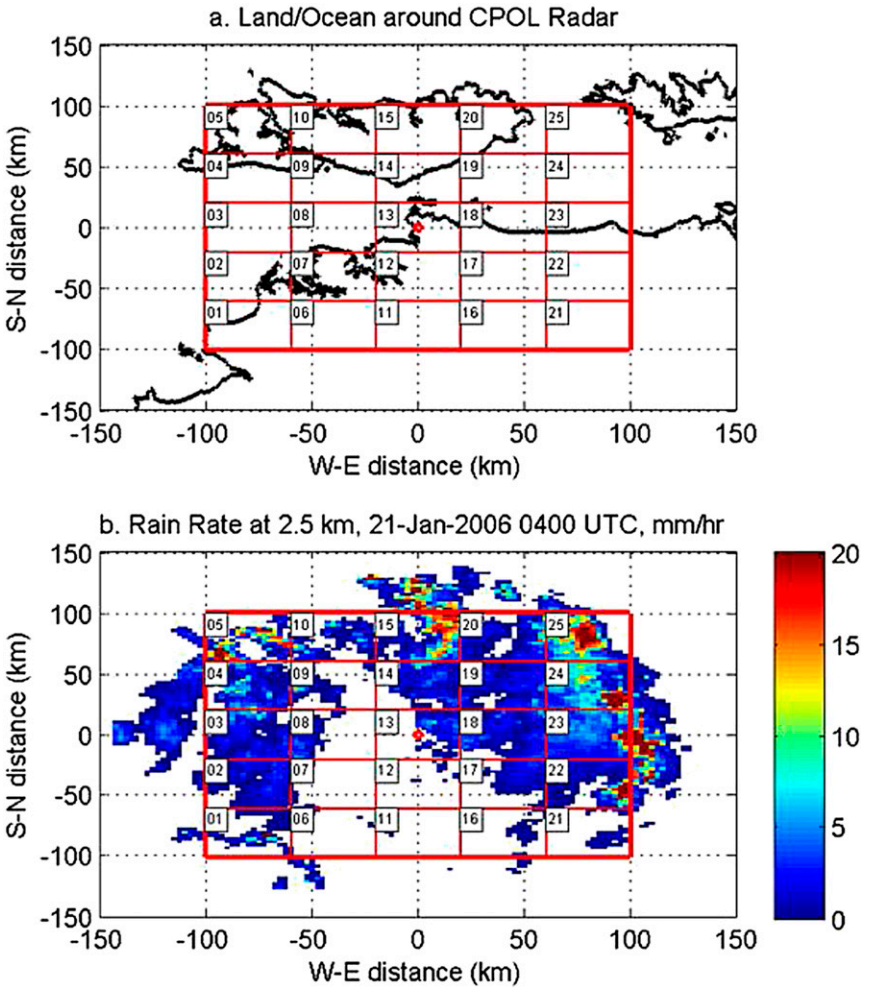

FIG. 1. (a) Sample grid boxes overlaid on a map of the coastlines. The red dot indicates the location of the radar. (b) Sample of CPOL rain-rate estimates (shaded; mm h^{-1}) at a horizontal resolution of 2.5 km and at a height of 2.5 km. The 5 × 5 matrix of boxes represents 25 grid boxes, each with a length and width of 40 km. The gridbox numbers are used in Fig. 2.

the interpolation. Note that prior to conversion to a uniform grid, Z_{dr} and the specific differential phase K_{dp} are filtered in range to reduce random fluctuations using a finite-impulse response filter (Hubbert and Bringi 1995; Bringi et al. 2009). At a range of 50 km, approximately 30 polar-coordinate samples are processed to estimate the reflectivity Z, median raindrop diameter D_0, and R for each 2.5-km square pixel. Because CPOL is a polarimetric radar, the rain rate is estimated using one of three functions depending on the observed Z, Z_{dr}, and K_{dp}. This estimation is performed using the threshold and decision tree described in Fig. 2 and Eqs. (1)–(5) in Bringi et al. (2009).

Because of Earth's curvature, scanning radars cannot observe close to the ground at large ranges. Thus, gridded rain rates are analyzed at a height of 2.5 km so that the observations extend to nearly 150 km from the radar, which is sufficiently large to define a 200-km square domain. Figure 1 shows an example of the CPOL rain rates estimated at a height of 2.5 km with a grid spacing of 2.5 km (Fig. 1a includes the coastlines for reference). The CPOL radar is located in the center of the grid; only pixels with rain rates of at least 0.07 mm h^{-1} are shown with color in Fig. 1. The CPOL minimum detectable signal at 150 km corresponds to a reflectivity of approximately 8.5 dBZ. To ensure uniform spatial statistics, only pixels with reflectivity of ≥8.5 dBZ were processed. This reflectivity corresponds to a minimum rain rate of 0.07 mm h^{-1} through the Z–R relationship defined by Eq. (5) in Bringi et al. (2009).

To highlight the analysis performed in this study, a 5 × 5 matrix of 40 km × 40 km grid boxes is superimposed on

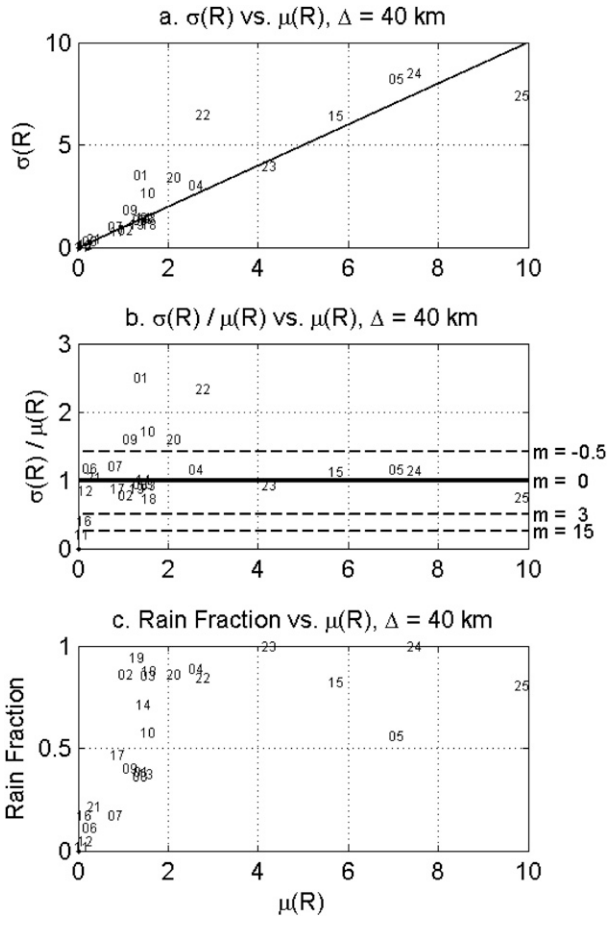

FIG. 2. Statistics calculated for the 40-km grid boxes shown in Fig. 1; the symbols correspond to the individual grid boxes. The statistics include (a) $\sigma(R)$ vs $\mu(R)$, (b) $\sigma/\mu(R)$ vs $\mu(R)$, and (c) f_R vs $\mu(R)$.

the rain rates shown in Fig. 1. The 40 km × 40 km grid boxes represent a numerical model with a 40-km spatial grid; the observed rain rates represent the subgrid-scale variability that cannot be explicitly resolved by a large-scale numerical model. For each grid box, several rain-rate statistics are calculated, including the conditional (within rain) mean rain rate $\mu(R)$, the conditional (within rain) rain-rate standard deviation $\sigma(R)$, and the rain fraction f_R. The ''conditional'' calculations imply that rain rates below a predefined minimum threshold (i.e., $R_{\min} = 0.07\,\text{mm h}^{-1}$) are omitted when estimating $\mu(R)$ and $\sigma(R)$. The rain-rate statistics are only computed for grid boxes in which at least 10% of the region contains precipitating pixels.

The rain-rate statistics for each of the 25 grid boxes depicted in Fig. 1 are shown as scatterplots in Fig. 2. The symbols used in each panel correspond to the grid numbers shown in Fig. 1. Figure 2a shows $\sigma(R)$ as a function of $\mu(R)$; the thin line indicates a 1:1 line. To help highlight deviations from the 1:1 line, Fig. 2b shows $\sigma/\mu(R)$ as a function of $\mu(R)$. As will be discussed in section 2c, this ratio provides information on the shape of the rain-rate distribution (for well-sampled distributions), in which a value of 1 corresponds to an exponential distribution (e.g., $m = 0$, where m is the shape parameter of a gamma distribution). Figure 2c shows the rain fraction as a function of $\mu(R)$. Note the correspondence between the calculated low rain fractions in Fig. 2c and the grid boxes with only a few raining pixels in Fig. 1.

In this study, each 200-km domain containing CPOL rain rates (and the modeled rain rates discussed in the next section) is resampled using grid boxes with dimensions ranging from 10 to 60 km to generate statistics of $\sigma(R)$, $\mu(R)$, and f_R as a function of spatial scale.

b. Model simulation

The Weather Research and Forecasting (WRF) Model is used to simulate the TWP-ICE intensive operating period (IOP). Input and forcing fields are obtained from Fridlind et al. (2010). The following assumptions are made with regard to the simulation (Fridlind et al. 2012). The sea surface temperature is fixed at 29°C. The horizontal boundaries are assumed to be periodic. Radiative forcing is applied to mimic the diurnal variation in insolation over the Darwin Atmospheric Radiation Measurement Program site. The simulation is run for 16 days (only 10 days of which are used in the subsequent analysis; more details follow in the next section). The horizontal winds are nudged above 500 m to observed profiles with a 2-h time scale. Large-scale advective forcings of potential temperature and water vapor are applied based on observations; these forcings are applied below 15 km and linearly decrease to zero at 16 km. The water vapor and potential temperature are nudged to observed profiles with a 6-h time scale; these fields are nudged above 16 km and linearly decrease to zero at 15 km.

The domain is 200 km × 200 km in the horizontal direction, extending to 24 km in the vertical direction. The horizontal grid spacing is 500 m, and the vertical grid spacing is approximately 100 m at the surface, 300 m at $z = 10$ km, and >1000 m above $z = 18$ km. The time step is permitted to vary between 1 and 16 s depending upon the Courant number at any given time step so that quiescent periods can be quickly simulated while maintaining numerical stability during more active periods. Both longwave and shortwave radiative fluxes are computed using the Rapid Radiative Transfer Model parameterization. A two-moment bulk microphysics scheme with fixed droplet number concentration ($100\,\text{cm}^{-3}$) is utilized in this study (Morrison et al. 2009). To test the

robustness of the results, an additional simulation with a higher droplet number concentration ($500\,\mathrm{cm}^{-3}$) was performed. The results of the two simulations were found to be largely indistinguishable when analyzed over the course of the IOP.

To generate consistent statistics between the modeled and observed rain rates, the model output is averaged to a 2.5-km horizontal grid at a height of 2.5 km. For the purpose of formulating parameterizations that can be readily implemented into large-scale models, the model-predicted rain rates and rainwater mixing ratios at the inherent model grid spacing (i.e., 500 m) are used. Last, all R and q_r are conditionally averaged by assuming $R_{\min} = 0.07\,\mathrm{mm\,h}^{-1}$, which corresponds to the minimum rain rate detected by the radar, and $q_{r,\min} = 0.0001\,\mathrm{g\,kg}^{-1}$.

c. *Theory describing expected $\sigma/\mu(R)$*

It is assumed that the rain-rate distribution $p(R)$ can be described by a gamma distribution (e.g., Cho et al. 2004):

$$p(R) = \frac{1}{\Gamma(m+1)\theta^{m+1}} R^m \exp(-R/\theta), \tag{1}$$

where m is the shape parameter, θ is the scale parameter, and $\Gamma()$ is the Euler gamma function. Assuming that the rain-rate field is sufficiently sampled, the expected mean $\mu(R)$ and variance $\sigma^2(R)$ can be defined as follows:

$$\mu(R) = (m+1)\theta \quad \text{and} \tag{2}$$

$$\sigma^2(R) = (m+1)\theta^2. \tag{3}$$

From these relationships, the ratio of $\sigma(R)$ to $\mu(R)$ can be written as

$$\sigma/\mu(R) = \sigma(R)/\mu(R) = (m+1)^{-1/2}. \tag{4}$$

Equation (4) shows that $\sigma/\mu(R)$ is an inverse function of the gamma shape parameter. In specific terms, for an exponential rain-rate distribution (i.e., where m is 0), the ratio is unity, and the ratio becomes less than unity as m increases. Equation (4) can be rearranged to solve for m:

$$m = \left[\frac{\sigma(R)}{\mu(R)}\right]^{-2} - 1, \tag{5}$$

suggesting that the shape parameter can be diagnosed from $\sigma/\mu(R)$. Alternatively, if $\mu(R)$ is known (e.g., prognosed in a large-scale model or retrieved from satellite observations) and one can determine $\sigma(R)$ based on a parameterization (this study), one may also be able to determine the shape parameter of the gamma distribution needed to fit the rain-rate distribution.

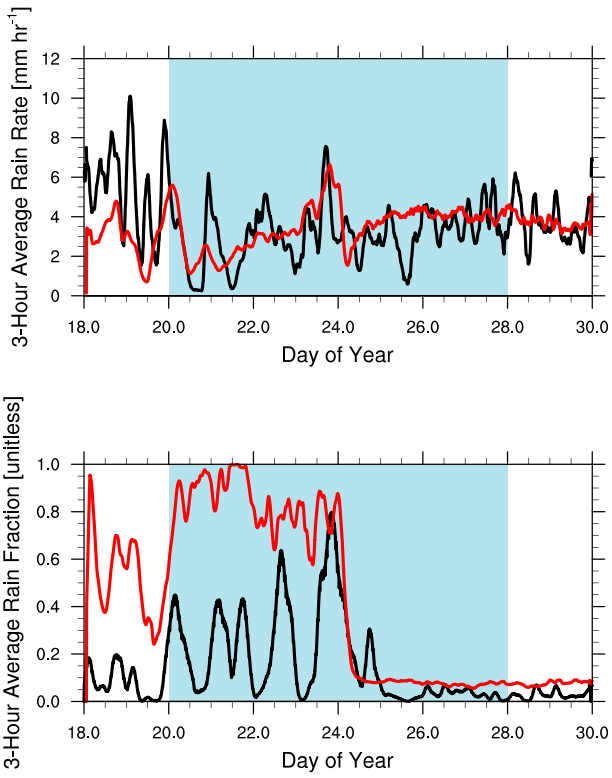

FIG. 3. The 3-h average (top) rain-rate and (bottom) rain-fraction time series for both the CPOL data (black) and the model output (red). The blue box corresponds to the period of focus in this study, encompassing both the active and suppressed phases of the summer monsoon.

3. Results

a. *Comparison between observations and model output at $z = 2.5$ km*

We first explore similarities and differences between the radar-retrieved and model-predicted rain rates, both area averaged to a 2.5-km horizontal grid at a height of 2.5 km (unless otherwise noted, the model output is discussed herein after performing area averaging). Figure 3 shows a time series of 3-hour-averaged radar-retrieved (black) and area-weighted model-predicted (red) rain rates at a height of 2.5 km. The blue box corresponds to the period selected for analysis herein. By neglecting the initial 48 h, we are assured that a sufficient amount of time is allowed for model spinup. The period encompasses 10 days. Overall, the two time series correspond well to one another. There are some differences in the rain fraction at any given time. As shown later, however, this overestimate in the rain fraction has little to no effect on the characteristics of the overall rain-rate distributions when compared with the radar data.

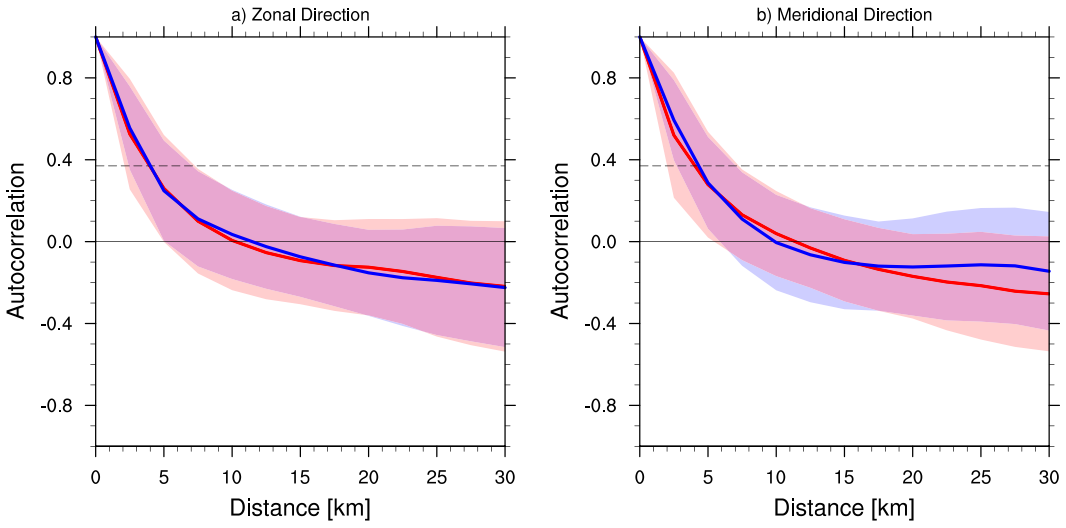

FIG. 4. Autocorrelation functions for the radar-estimated rain rates (blue) and model-predicted rain rates (red) at a height of 2.5 km in the (a) zonal and (b) meridional directions. The shading denotes ±1 standard deviation.

Figure 4 shows a comparison of the autocorrelation functions, which provide a sense of the spatial correlation of the investigated fields. For the purpose of this study, the autocorrelation functions are calculated only for linear bands of rain that contain at least 10 contiguous raining points. The calculation is performed for linear bands in both the zonal and meridional directions to explore the potential for asymmetry in the spatial pattern of precipitation in either the radar data or the model output. The thin horizontal line corresponds to a value of e^{-1}; therefore, the point at which the autocorrelation function crosses this threshold represents the e-folding distance. Again, we find fairly good agreement between the model output and the observations at a height of 2.5 km. Moreover, there tends to be good agreement in the autocorrelation functions in the zonal and meridional directions, suggesting an e-folding distance of 4–5 km and complete decorrelation at a distance of 10–12 km.

Figure 5 shows PDFs of R [or $\mu(R)$ for the resampled datasets] for both the inherent resolution of the radar data and the model output and for different sampling footprints (Table 1) (note that the data are only spatially averaged; no temporal averaging is performed). Again, we find good agreement between the radar-retrieved R and the model-estimated R even across a wide range of footprint sizes Δ. The PDFs suggest that the distribution of R is superexponential for small Δ. As Δ increases, the PDFs become more exponential in nature. This shift in the shape of the R PDFs highlights the fact that $\sigma/\mu(R)$ varies as a function of Δ or, in other words, that $\sigma/\mu(R)$ is scale dependent.

Agreement in the PDFs of R for different sampling footprints provides some confidence that the model is capable of predicting the observed rain-rate field at a height of 2.5 km, although such distributions provide only qualitative information on the variability of R within a sampling footprint. We choose to use the standard deviation of the rain rate [i.e., $\sigma(R)$] to represent the variability within a box. Unless otherwise noted, all values of $\sigma(R)$ and $\mu(R)$ are conditionally averaged over raining regions of a given footprint. While dimensional reasoning may suggest that there should be a direct linkage between $\mu(R)$ and $\sigma(R)$, especially if the R distribution is exponential (in which case the ratio of these two quantities is identical to 1), we can exploit the radar data and model output to investigate other potentially important variables that explain the variability in R—for example, the rain fraction f_R. To do so, we computed Spearman's rank correlation coefficients between $\sigma(R)$ and both $\mu(R)$ and f_R (at a height of 2.5 km). A common alternative is the use of Pearson's correlation coefficients; however, because of the nonlinear nature of the resulting relationships, Spearman's rank correlation coefficients provide a more robust measure of correlation that is based on the monotonicity of a given relationship. The results are listed in Table 2. The values suggest that $\mu(R)$ is highly correlated with $\sigma(R)$ in both the model output and radar data (with similar correlation coefficients for the different footprint sizes). On the contrary, very weak positive and negative correlations are found between f_R and $\sigma(R)$, suggesting that the addition of this variable to the regressions discussed below has little to no added value in constraining $\sigma(R)$.

To investigate further the relationship between $\sigma(R)$ and $\mu(R)$ and to elucidate additional evidence to

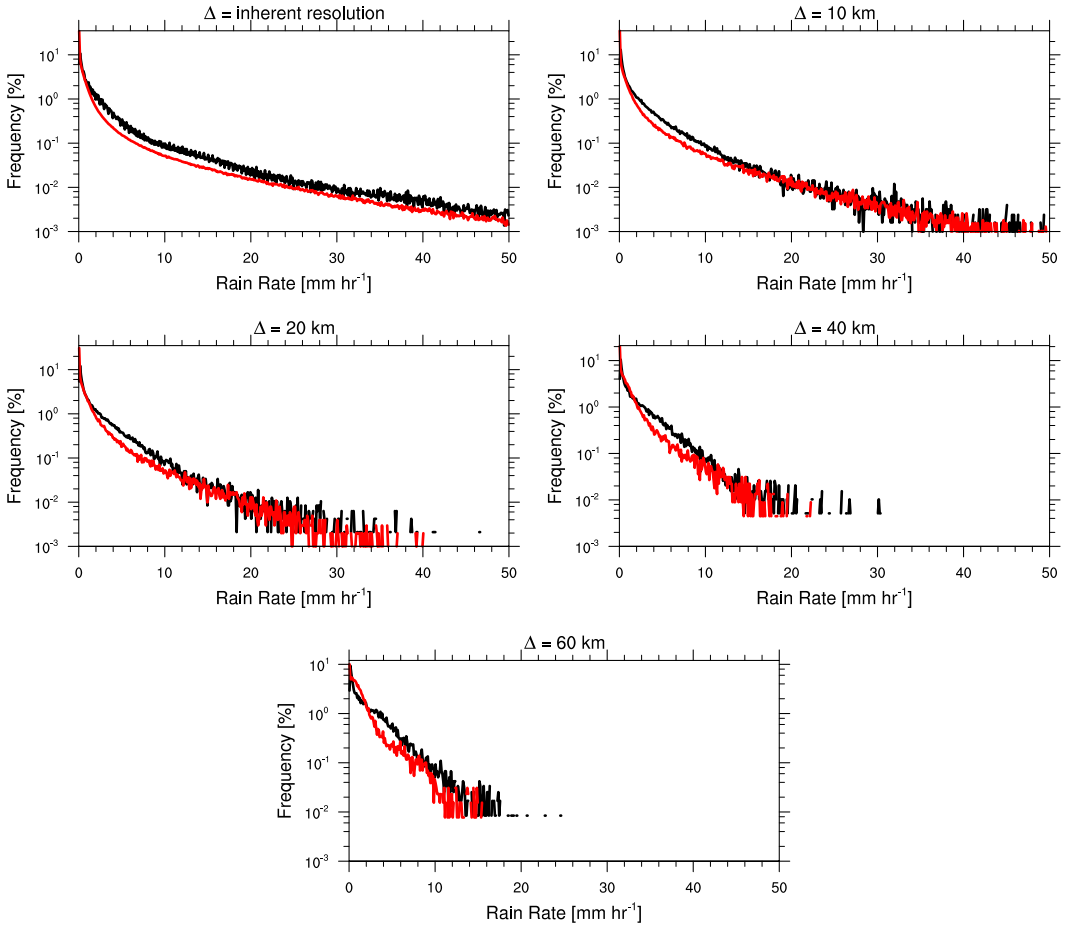

FIG. 5. Rain-rate PDFs for (top left) the entire domain and different sampling footprints. Shown are sampling footprints for Δ of (top right) 10, (middle left) 20, (middle right) 40, and (bottom) 60 km, including both the CPOL data (black) and the model output (red).

demonstrate the overall good agreement between the area-weighted model output and the radar data, we first present a set of figures depicting $\sigma/\mu(R)$ as a function of $\mu(R)$ for various footprint sizes (Fig. 6) at a height of 2.5 km. Again, there is good agreement between the radar and model-derived joint PDFs. Note that these are not subgrid-scale PDFs but rather histograms that were created using a single value of $[\sigma/\mu(R), \mu(R)]$ for each sampled footprint. The following inferences can be made from Fig. 6:

1) At small Δ, the most frequently occurring values are $\sigma/\mu(R) < 1$ for $\mu(R) < 1\,\text{mm h}^{-1}$ based on the model output and $\sigma/\mu(R)$ of 0.2–2 for $\mu(R)$ between 0.2 and $10\,\text{mm h}^{-1}$ based on the observations. These ranges are determined using the yellow and red regions depicted in Figs. 6a and 6b.
2) For small footprint sizes, $\sigma/\mu(R)$ is typically less than 1; as the footprint size increases, the ratio increases, approaching a mode of approximately 1.5–2 for both the observations and the model output. If one

TABLE 1. Number of domains per radar scan and number of pixels in each domain for different square domain lengths.

Footprint (sample) width/length (km)	Footprints per radar scan	Pixels per footprint (radar)	Footprints per model output	Pixels per footprint (model)
60	9	576	9	14 400
40	25	256	25	6400
20	100	64	100	1600
10	400	16	400	400

TABLE 2. Spearman's rank correlation coefficients. All correlations are calculation between the variables listed [i.e., $\mu(R)$ and f_R] and $\sigma(R)$.

	$\mu(R)$ for model	$\mu(R)$ for radar	f_R for model	f_R for radar
$D = 10$ km	0.93	0.94	0.12	0.21
$D = 20$ km	0.94	0.96	−0.04	0.16
$D = 40$ km	0.94	0.95	−0.20	0.06
$D = 60$ km	0.93	0.95	−0.24	0.05

assumes that the rain-rate distribution is gammalike, a value of 1 corresponds to the special case of an exponential distribution within a sampled grid box. The asymptotic behavior [i.e., reduced spread in the ratio of $\sigma(R)$ to $\mu(R)$ and convergence to a single mode for increasing Δ] is because the sampled grids contain a sufficient number of points to construct a distribution without substantial truncation or gaps; in other words, Δ is substantially larger than the decorrelation length presented in Fig. 4.

3) The joint PDFs asymptotically approach (0, 0) for small rain rates; this is an artifact of the lower threshold used to conditionally average R (i.e., 0.07 mm h^{-1}). Because a lower bound is applied, the only way for the mean to be equivalent to the lower bound is if *all* points within a sampled grid have a rain rate identical to the lower threshold; in this case, the standard deviation is identical to 0.

The correlations presented in Table 2 suggest that f_R is very weakly (at best) correlated with $\sigma(R)$. To demonstrate this relationship, we present joint PDFs of $\sigma/\mu(R)$ as a function of f_R in Fig. 7 for both the model output and radar data at a height of 2.5 km. The threshold used to determine f_R is identical to that used to determine both $\sigma(R)$ and $\mu(R)$ (i.e., 0.07 mm h^{-1}). The distributions determined from the model output and radar data agree fairly well. Unlike the relationship for $\sigma/\mu(R)$ as a function of $\mu(R)$, however, we find no robust behavior in $\sigma/\mu(R)$ as a function of f_R. There is a region of high occurrence [corresponding to small $\sigma/\mu(R)$ and small f_R] that corresponds well to the region of high occurrence for $\sigma/\mu(R)$ as a function of $\mu(R)$; beyond the region of maximum occurrence frequency, the relationship quickly breaks down. For $f_R > 0.15$, it is equally possible for $\sigma/\mu(R)$ to be between 0.5 and 4 based on the model output and between 0.5 and 2.5 based on the radar data. Given this large spread in $\sigma/\mu(R)$ over such a wide range of f_R, a robust relationship between these quantities is unlikely.

To bring us one step closer to the goal of formulating a parameterization for $\sigma(R)$ at the surface, joint PDFs of $\sigma(R)$ as a function of $\mu(R)$ using the model output and radar data rounded to the same precision are depicted in Fig. 8 (unlike Fig. 6, which was on a linear–linear plot, this figure has log–log axes). The 1:1 line is shown (dashed black) for guidance. In addition, a nonlinear regression is performed on both the model output and the radar data to obtain fitting functions for $\sigma(R)$ as a function of $\mu(R)$ (red) using a power-law function:

$$\sigma = a\mu^b, \tag{6}$$

where a has units of "(mm h^{-1})$^{1-b}$" and b is unitless [$\sigma(R)$ and $\mu(R)$ both have units of millimeters per hour]. Unlike the $\sigma/\mu(R)$ relationship with $\mu(R)$, $\sigma(R)$ as a function of $\mu(R)$ is more robust and, when plotted on a log–log plot, the relationship is nearly linear. The only exception to this finding is for low $\mu(R)$ (i.e., near $R_{\min}$) in which $\sigma(R)$ approaches 0. This decrease is again an artifact of imposing a lower bound on R. In any case, these points are very infrequent relative to the region of maximum frequency of occurrence; therefore, the outliers exhibit little weight in the nonlinear regression analysis. In addition, an examination of $\sigma(R)$ as a function of $\mu(R)$ is more reasonable because $\sigma/\mu(R)$ can attain very large or small values at the extremes.

While the power-law relationship in Eq. (6) represents a line passing through the observations or simulations, the spread around the best-fit line can be quantified in two different ways. First, the spread could be quantified by estimating error bars for both fitted power-law parameters. Alternatively, the observational spread around the best-fit line could be quantified using PDFs. This study uses the latter method and estimates PDFs of the coefficient a around the best fit by determining the normalized coefficient a' (Haddad et al. 1996):

$$a' = \sigma(R)/\mu(R)^b. \tag{7}$$

This normalization accounts for the power-law curve in which a' represents the distance from the best-fit line. The a' mean value is close in magnitude to the derived coefficient, although the two quantities are not identical because the normalization performed in Eq. (7) is different than the original power-law fitting method. In addition, the spread in a' represents the spread in the observations while maintaining a constant exponent in the power-law relationship (i.e., b). Figures 9a and 9b show the distribution of a' as normalized PDFs for the model and CPOL observations, respectively. The statistics of these a' distributions are listed in Table 3.

b. *Determining a parameterization for $\sigma(R)$ at the surface*

The previous analysis focused on a direct comparison of model output and radar observations at a height of

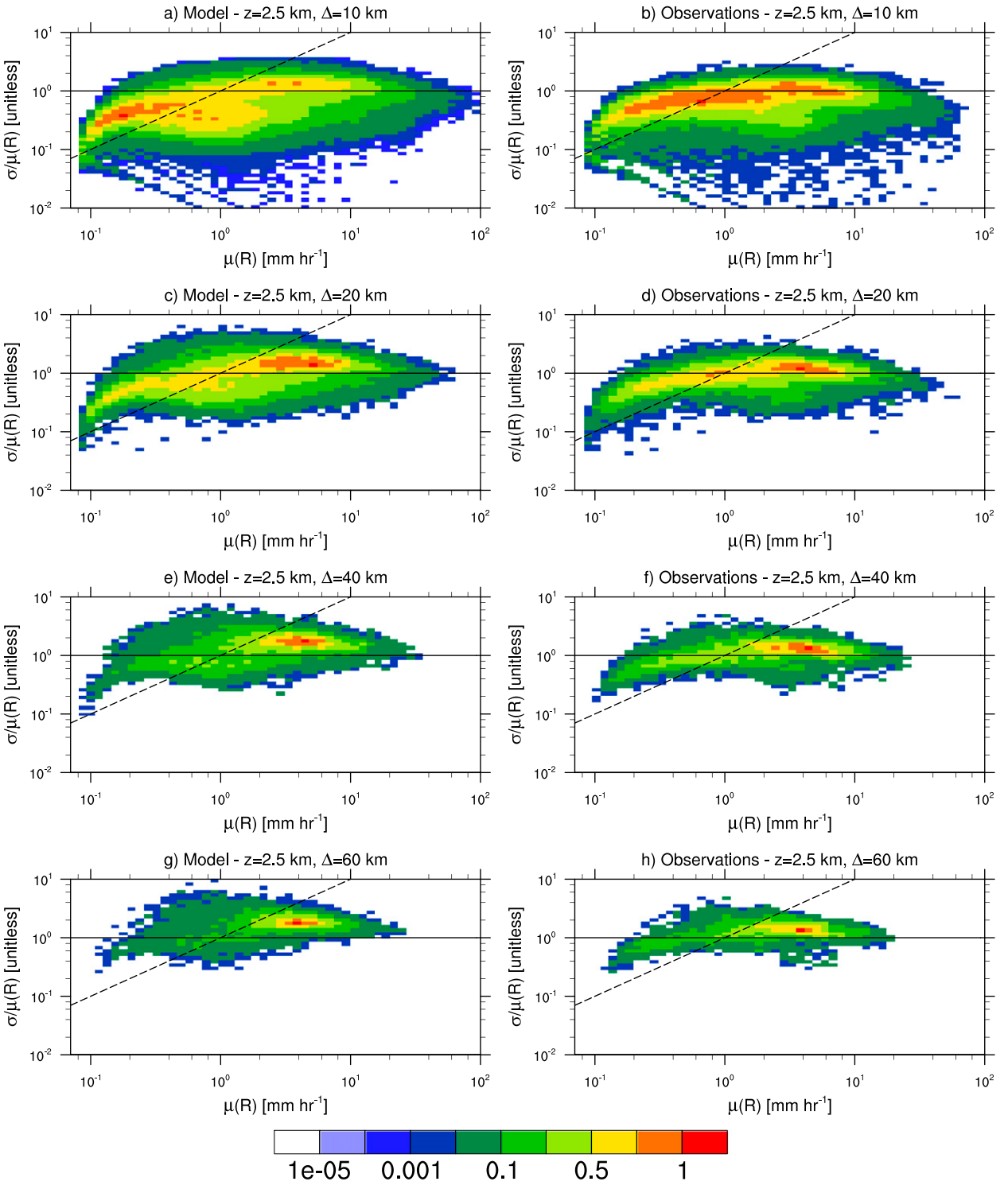

FIG. 6. Normalized joint PDFs of $\mu(R)$ (x axes) and $\sigma/\mu(R)$ (y axes) for different sampling footprints, i.e., (a),(b) $\Delta = 10$ km, (c),(d) $\Delta = 20$ km, (e),(f) $\Delta = 40$ km, and (g),(h) $\Delta = 60$ km. The frequencies are normalized to aid in the comparison of (left) model output and (right) the CPOL data. The 1:1 line (dashed) and $\sigma/\mu = 1$ (i.e., indicative of an exponential distribution; solid) are also depicted for guidance.

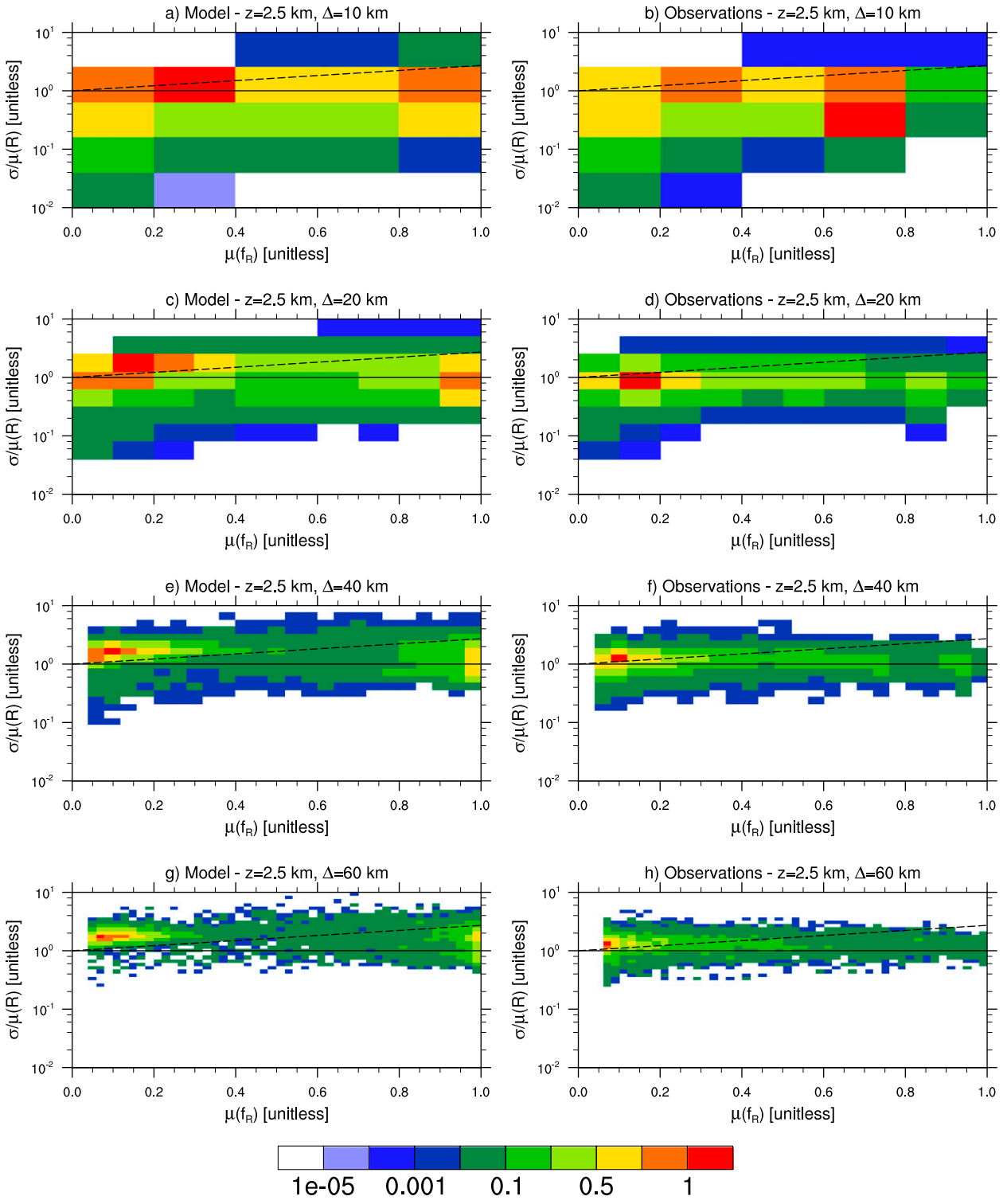

FIG. 7. Normalized joint PDFs of f_R (x axes) and $\sigma/\mu(R)$ (y axes) for different sampling footprints, i.e., (a),(b) $\Delta = 10$ km, (c),(d) $\Delta = 20$ km, (e),(f) $\Delta = 40$ km, and (g),(h) $\Delta = 60$ km. The frequencies are normalized to aid in the comparison of (left) the model output and (right) the CPOL data. Because there are a finite number of values for f_R at any given Δ, the number of bins used to calculate the PDFs ranges from 5 ($\Delta = 10$ km) to 50 ($\Delta = 60$ km).

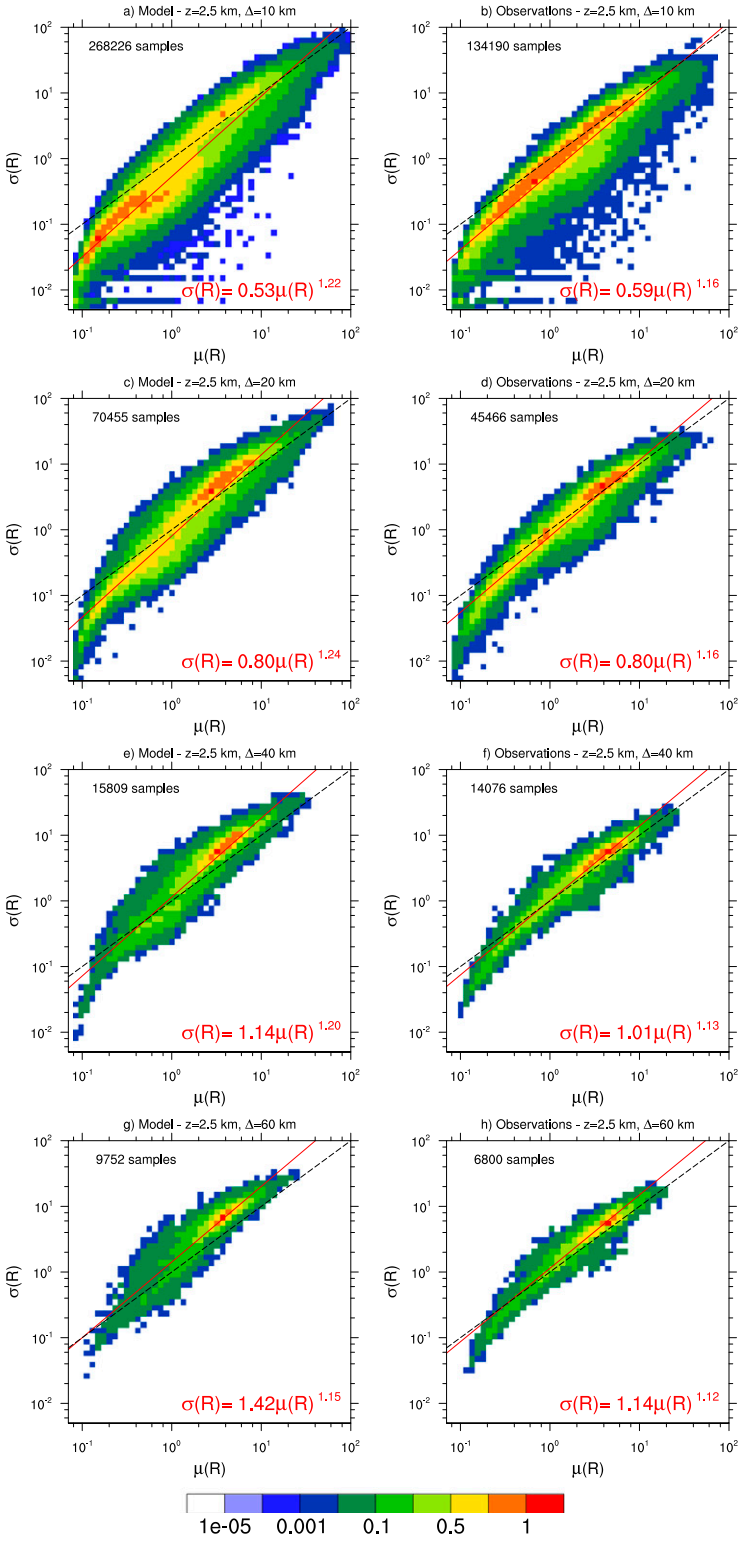

FIG. 8. Normalized joint PDFs of $\mu(R)$ (x axes) and $\sigma(R)$ (y axes) for different sampling footprints, i.e., (a),(b) $\Delta = 10$ km, (c),(d) $\Delta = 20$ km, (e),(f) $\Delta = 40$ km, and (g),(h) $\Delta = 60$ km. The frequencies are normalized to aid in the comparison of (left) model output and (right) the CPOL data. The 1:1 line (dashed black) and fitted power-law model (red solid) are also shown.

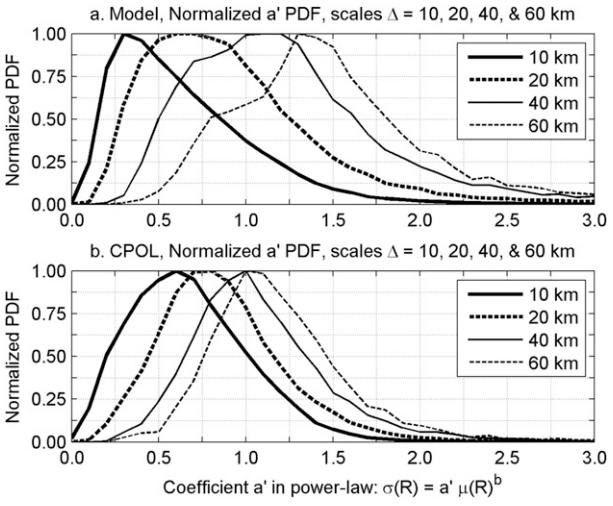

FIG. 9. Normalized PDF of a' calculated for each power-law relation at scales of 10, 20, 40, and 60 km. The distributions are shown for (a) the model simulations and (b) the CPOL observations. The prime denotes the uncertainty in the fits.

2.5 km, suggesting good overall agreement between the two different datasets. A parameterization of *surface* rain-rate variability may be more applicable for other applications, for example, hydrometeorological studies. Therefore, we employ the model-predicted surface rain rates at the inherent grid spacing (i.e., the output is not area averaged to correspond to the grid spacing used for the radar data) to formulate a rain-rate parameterization that can be easily implemented into large-scale models.

Figure 10 portrays the joint PDFs for $\sigma(R)$ and $\mu(R)$ at the surface based on the model output. As was the case at a height of 2.5 km, the joint PDFs suggest a power-law relationship between $\sigma(R)$ and $\mu(R)$ at the surface. The fitted formulations are shown in the lower right-hand corner of each panel [again, for $\sigma(R) = a\mu(R)^b$, where b is unitless and a has units of "$(\text{mm h}^{-1})^{1-b}$"].

To illustrate and parameterize the scale-dependent nature of the $\sigma(R)$–$\mu(R)$ relationship, the parameters of the power-law relationships are presented as a function of Δ in Fig. 11 using the following linear relationships:

$$a = x_1 + m_1\Delta \quad \text{and} \tag{8}$$

$$b = x_2 + m_2\Delta. \tag{9}$$

The parameters of these relationships are fit using ordinary least squares; the following values are obtained (units are in square brackets):

$$x_1 = 0.54 \quad [(\text{mm hr}^{-1})^{1-b}], \tag{10}$$

$$m_1 = 2.12 \times 10^{-2} \quad [(\text{mm hr}^{-1})^{1-b}\,\text{km}^{-1}], \tag{11}$$

$$x_2 = 1.31 \quad [\text{unitless}], \quad \text{and} \tag{12}$$

$$m_2 = -2.97 \times 10^{-3} \quad [\text{km}^{-1}]. \tag{13}$$

Figure 11 nicely illustrates that the exponent is fairly similar for all Δ (red; slope of $-0.002\,97\,\text{km}^{-1}$). The monotonic and essentially linear increase in the coefficient is also nicely illustrated [black; slope of 0.0212 km $(\text{mm h}^{-1})^{1-b}\,\text{km}^{-1}$].

As shown in section 3b, $\sigma/\mu(R)$ can be used to determine m (i.e., the shape parameter) of the rain-rate gamma distribution. Equation (6) can be rewritten as follows:

$$\sigma/\mu(R) = a\mu^{b-1}. \tag{14}$$

Inserting this equation into Eq. (5) results in the following expression for m as a function of $\mu(R)$:

$$m = (a^2\mu^{2b-2})^{-1} - 1. \tag{15}$$

Then, the formulations for a and b shown in Fig. 11 can be used here to determine a scale-dependent formulation for m as a function of $\mu(R)$.

TABLE 3. Statistics describing the distribution of the coefficient a' in the power-law relation $\sigma(R) = a'\mu(R)^b$. The statistics include the mean μ, standard deviation σ, and skewness γ_1 for a'. Also shown are the 10th, 25th, 50th (median), 75th, and 90th percentiles.

	Fitted parameters		Statistics of $a' = \sigma(R)^b$							
Footprint scale	a	b	μ	σ	γ_1	10%	25%	50%	75%	90%
Model simulations										
10 km	0.53	1.22	0.65	0.41	1.37	0.22	0.34	0.56	0.87	1.20
20 km	0.80	1.24	0.93	0.54	1.77	0.38	0.56	0.83	1.16	1.57
40 km	1.14	1.20	1.28	0.66	1.63	0.62	0.84	1.16	1.53	2.05
60 km	1.42	1.15	1.55	0.70	1.47	0.84	1.12	1.43	1.79	2.33
CPOL observations										
10 km	0.59	1.16	0.68	0.34	0.64	0.27	0.43	0.65	0.89	1.14
20 km	0.80	1.16	0.87	0.36	0.96	0.45	0.62	0.83	1.06	1.34
40 km	1.01	1.13	1.09	0.41	1.39	0.65	0.82	1.02	1.28	1.58
60 km	1.14	1.12	1.20	0.42	1.50	0.77	0.94	1.14	1.40	1.70

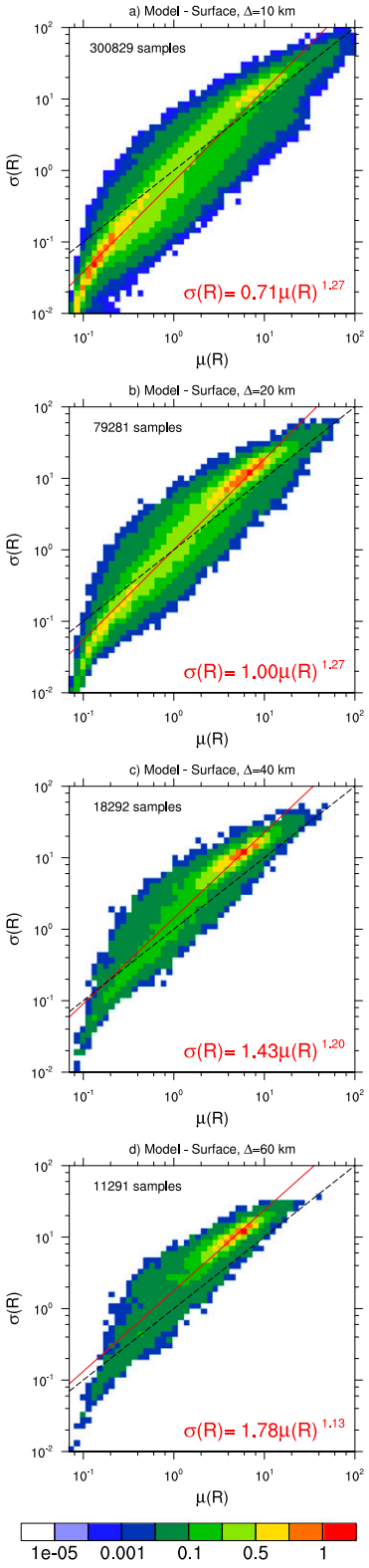

FIG. 10. As in Fig. 8, but for the inherent model resolution at the surface.

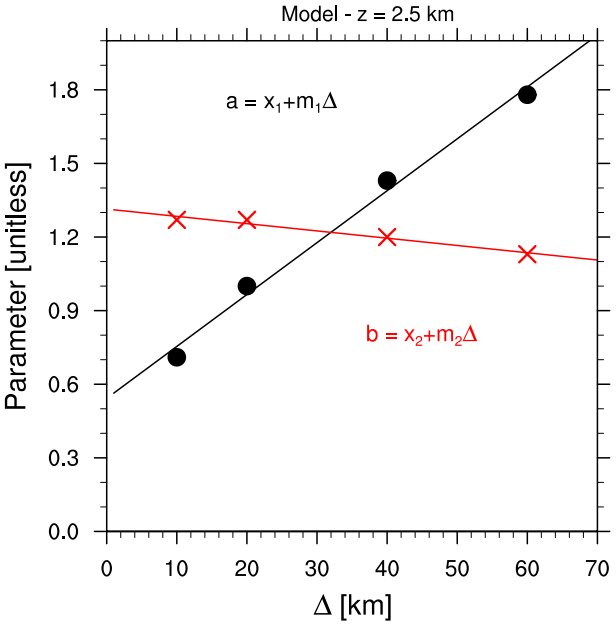

FIG. 11. Fitting parameters a (red) and b (black) as a function of Δ based on the output of the high-resolution model at the surface. The values of x_1, x_2, m_1, and m_2 are given in Eqs. (10)–(13).

c. *Discussion*

Figure 8 illustrates two important results. 1) The exponent in the power-law relationship is nearly constant for *all* footprint sizes and appears to be largely consistent between model output and radar data. 2) The coefficient in the power-law relationship *increases* with increasing footprint size, suggesting that the relationship between $\sigma(R)$ and $\mu(R)$ is scale dependent. For $\Delta = 10$ km, the points within the footprint tend to be correlated (see Fig. 4); hence, a complete PDF is not attainable for such a small footprint size. As Δ increases, a more complete PDF can be obtained within the sampled region. For increasingly large Δ (i.e., beyond that which is shown herein), the power-law fits approach that attained when randomly sampling points in the domain (i.e., the case in which the rain rate is spatially uncorrelated).

To better illustrate the previous notion, Fig. 12 depicts the joint PDFs of $\sigma(R)$ and $\mu(R)$ and the corresponding power-law fits in which the sampling is completely random (e.g., 400 points are randomly selected from the model output at a specific time for $\Delta = 10$ km; this process is repeated N times, where N is the number of sampling footprints obtained using regular square footprints listed in Table 1). In this case, Δ does not represent a spatially cohesive portion of the domain; instead, each footprint of size Δ is composed of the same number of randomly selected points from the domain

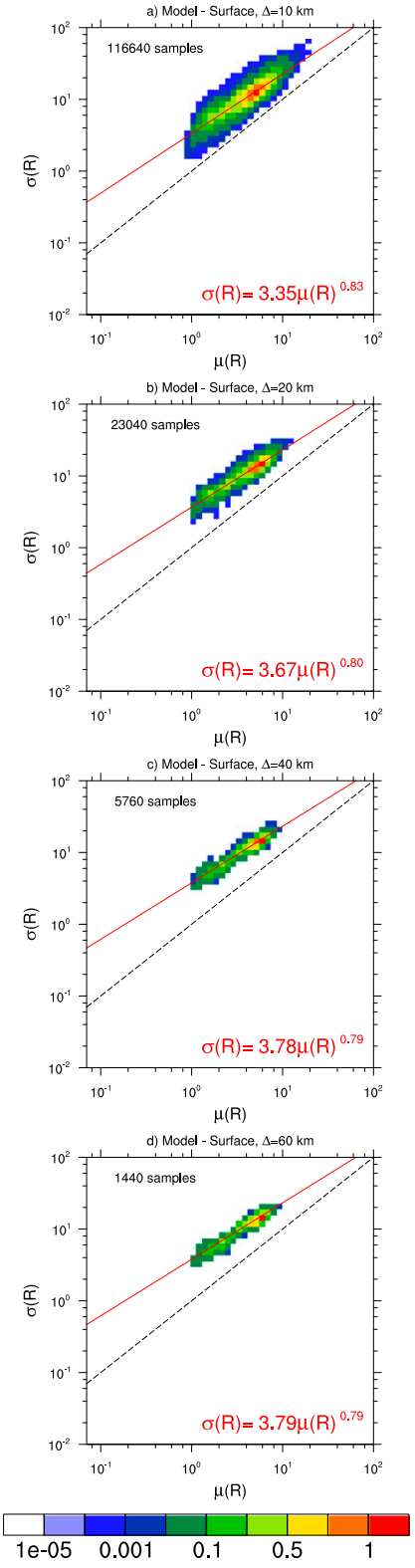

FIG. 12. As in Fig. 8, but for random samples.

at a given instance in time (with replacement) to generate N samples that mimic a footprint of size Δ except with no spatial correlation between adjacent points. We find that both the coefficient and the exponent of the fitted power-law relationships are nearly invariant as a function of Δ (the leading coefficient is slightly smaller for $\Delta = 10$ km, suggesting that more points are needed to sufficiently sample the rain-rate PDF). If the rain-rate field is spatially uncorrelated, the fitted power-law functions are not scale dependent. In addition, large regions of light precipitation are completely removed by randomly sampling the domain because it is unlikely that the random sampling will result in contiguous pixels with only light precipitation, which results in an increase in both the leading coefficient and the exponent of the fitted power-law relationships. By comparing Figs. 8 and 12, one sees that as Δ increases, the fits based on the actual model output approach those for the randomly sampled model output.

Another aspect of the results presented herein that deserves discussion is the difference in the power-law coefficients between the area-averaged model output at a height of 2.5 km (Fig. 8) and the model output at the surface (Fig. 10); the coefficients are higher at the surface. The reason for this difference is not related to the difference in the analysis being performed at the surface versus a height of 2.5 km. Instead, the differences are due to the area averaging that is performed on the model output. By area averaging the model output at a height of 2.5 km, $\mu(R)$ remains constant for a given footprint size while $\sigma(R)$ decreases. This artifact of the area averaging results in artificially lower $\sigma(R)$ and lower coefficients in the fitted power-law relationships (note that the surface rain rates are not area averaged for the purpose of formulating a parameterization of rain-rate variability). This conclusion was confirmed by recalculating the fits at all levels at or below a height of 2.5 km using the raw model output (i.e., at the inherent grid spacing). These fits were found to be nearly identical to those obtained at the surface (not shown), suggesting that the scale-dependent fits presented in Fig. 11 may be invariant between the surface and a height of 2.5 km.

4. Vertical profiles of $\sigma(R)$ and $\sigma(q_r)$

In addition to constraining the spatial variability of R at the surface, an understanding of how the variability changes with height has important implications for, for example, analyzing cloud-base rain rate. Moreover, a representation of the variability in $\sigma(q_r)$ is useful for constraining unified cloud models, as discussed in detail in the introduction. To address these points, the analysis

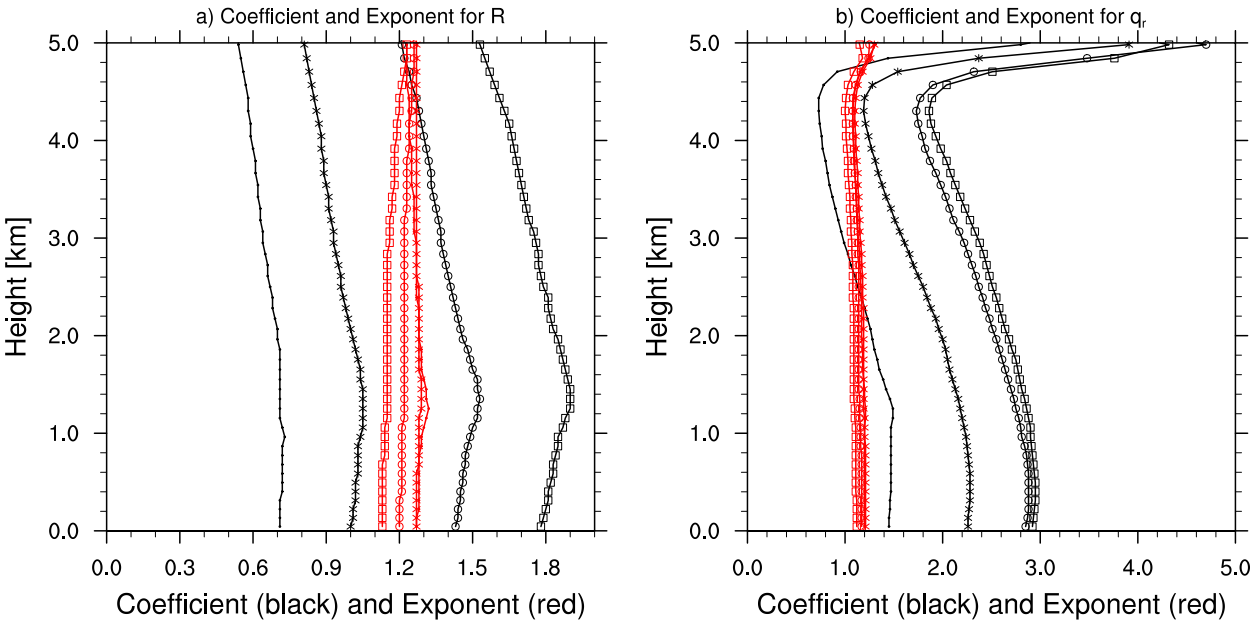

FIG. 13. Profiles of the power-law parameters, i.e., the leading coefficient (black) and exponent (red) for the (a) rain rate and (b) rainwater mixing ratio as a function of height. The different averaging areas are denoted as follows: Δ of 10 (dots), 20 (asterisks), 40 (circles), and 60 (squares) km.

presented in the previous section is repeated for both R and q_r at all model levels below 5 km. The reason for putting a threshold of 5 km on the analysis is because this location roughly corresponds to the melting level; the rain fraction quickly approaches 0 at levels above this height, resulting in inadequate statistics.

Each joint PDF is fitted using a power-law function, and the corresponding coefficients and exponents are shown in Figs. 13a and 13b. With regard to q_r, the fitted coefficient is smallest just below the melting level, which is due to the large source of rain from the melting of graupel and/or snow. As expected, the coefficient is smallest for the smallest Δ and increases with increasing Δ (see section 3c). As one moves downward, the coefficient increases monotonically (except for a slight deviation from monotonicity near the surface). If the exponent of the fitted power-law relationships were uniformly identical to 1 at all levels, we could use the leading coefficient to understand how the variability changes with height. However, the exponents exceed 1 for both R and q_r at all levels. For R, the exponent decreases as one moves downward, whereas for q_r, the exponent tends to increase as one moves downward. Moreover, the profiles of the leading coefficients for R and q_r exhibit different characteristics shapes.

To examine further the differences in the profiles of the fitted coefficients and exponents, we show the average of the within-rain footprint-scale means and standard deviations for R and q_r in Fig. 14. It is important to remember that these profiles are not domain averages; instead, they depict the average of the conditionally averaged means and standard deviations within each averaging region. According to these profiles, the footprint-scale $\mu(q_r)$ increases rapidly below the melting level, becomes nearly constant with height, and then decreases toward the surface. Moreover, $\sigma(R)$ simply increases down to a height of approximately 2.4 km for all Δ before decreasing toward the surface. When examining the relative standard deviation $\sigma/\mu(q_r)$ (Fig. 14c), however, the characteristic shape of the fitted leading coefficient in the power-law relationships shown in Fig. 13b is obtained, indicating that the coefficient of the power-law fit is indicative of the relative dispersion in the q_r field. The same conclusion can be made for R by comparing with Fig. 14g. Moreover, if we use the fitted coefficients and exponents shown in Fig. 13 to estimate $\sigma(q_r)$ and $\sigma(R)$ based on the mean profiles shown in Figs. 14a and 14e, we obtain the characteristic profiles of the relative dispersion, demonstrating that the fitted relationships are capable of representing the model-predicted variability in both the q_r and R fields.

To represent the results presented in Fig. 13 quantitatively, the coefficients and exponents are fitted to linear functions of Δ at several levels, which is similar to the analysis that was conducted in the previous section, resulting in the parameterization outlined in Fig. 11 and Eqs. (8)–(13). In this case, however, the parameters (i.e., m_1, m_2, x_1, and x_2) are functions of z. These

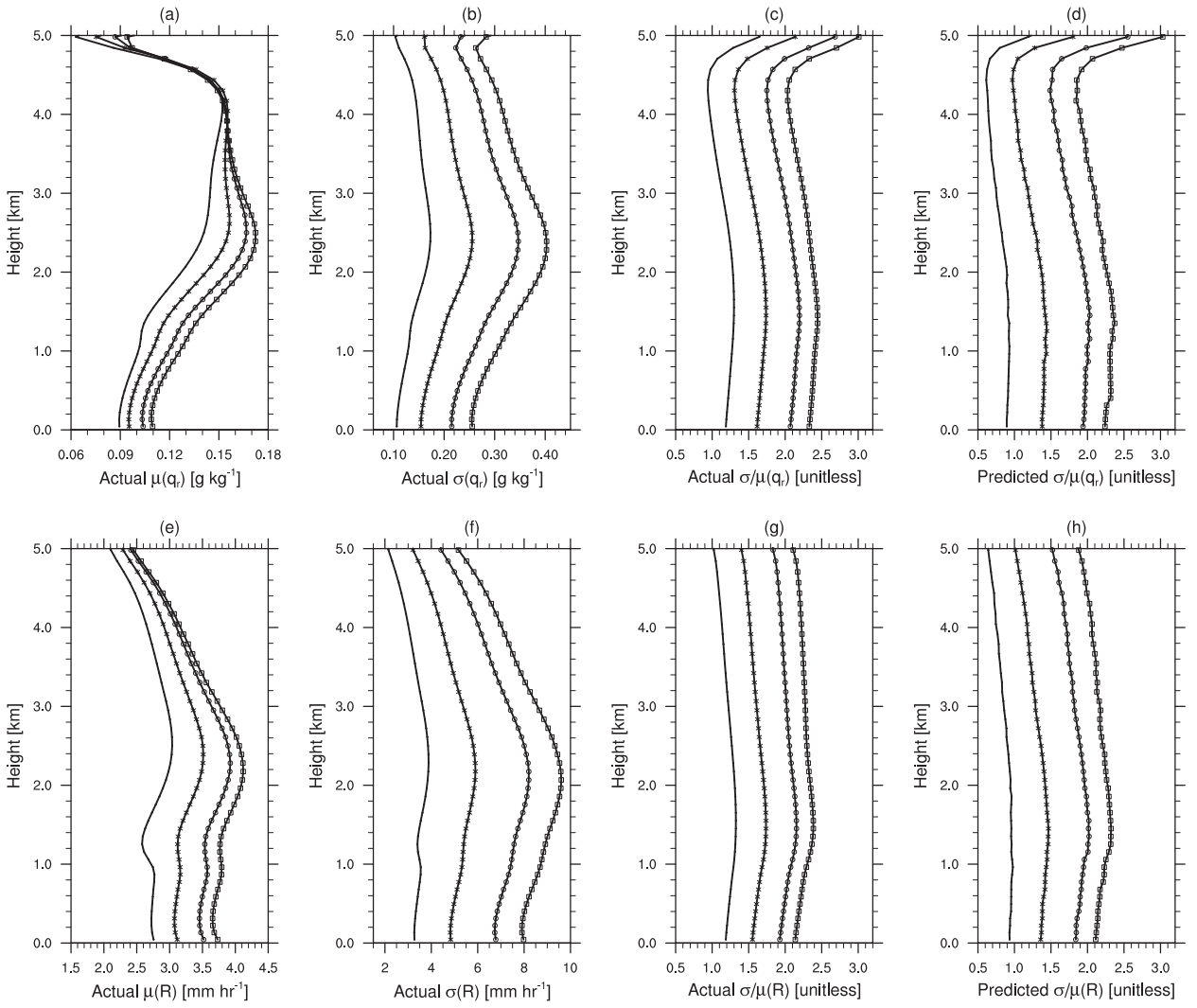

FIG. 14. Average of the within-rain footprint-scale (a),(e) means and (b),(f) standard deviations. Also shown is the ratio σ/μ based on (c),(g) the model output and (d),(h) using the parameterization defined in Tables 4 and 5. Shown are (top) q_r and (bottom) R. The different footprint sizes are denoted as follows: $\Delta = 10$ (solid line), 20 (asterisks), 40 (open circles), and 60 (open squares) km.

height-dependent parameters are listed in Tables 4 and 5. Note that these height-dependent parameters are based on the tropical case explored in this study.

The results presented in Figs. 13 and 14—in particular, the differences in the profiles of $\mu(R)$ and $\mu(q_r)$—are particularly intriguing and warrant a mechanistic explanation. The processes controlling q_r are not necessarily identical to those controlling R. For example, q_r can increase below the melting level because of the addition of graupel and/or snow that melts and can decrease because of evaporation. These processes have similar effects on R. Self-collection of raindrops has no effect on q_r but acts to *increase* R (mean drop size increases, which acts to increase the raindrop terminal fall speeds). In addition, air density increases as one moves downward, which can also result in a more rapid change in R when compared with that of q_r. These are likely the reasons that $\mu(R)$ does not decrease as rapidly as q_r below approximately 2.4 km.

5. Conclusions

Radar-retrieved and model-predicted estimates of R for the TWP-ICE IOP are used herein to evaluate subgrid-scale variability in R for a variety of scales and to formulate a parameterization for the surface variability in R that can be used in large-scale modeling frameworks, for example, CLUBB. The model output is further explored to provide scale- and height-dependent relations for the spatial variability of both

TABLE 4. Scale-dependent parameter values for the fitted power-law relation used to predict the spatial variability of q_r.

	$\sigma[q_r(z)] = a(z)\mu[q_r(z)]^{b(z)}$			
	$a(z) = m_1(z)\Delta + x_1(z)$ $[(\mathrm{g\,kg^{-1}})^{1-b}]$		$b(z) = m_2(z)\Delta + x_2(z)$ (unitless)	
z (m)	$m_1(z)$ $[(\mathrm{g\,kg^{-1}})^{1-b}\,\mathrm{km^{-1}}]$	$x_1(z)$ $[(\mathrm{g\,kg^{-1}})^{1-b}]$	$m_2(z)$ $(\mathrm{km^{-1}})$	$x_2(z)$ (unitless)
250	2.80×10^{-2}	1.48	-1.73×10^{-3}	1.23
750	2.74×10^{-2}	1.49	-1.92×10^{-3}	1.23
1250	2.61×10^{-2}	1.47	-2.19×10^{-3}	1.23
1750	2.69×10^{-2}	1.31	-1.97×10^{-3}	1.21
2250	2.62×10^{-2}	1.18	-1.81×10^{-3}	1.21
2750	2.68×10^{-2}	1.00	-1.58×10^{-3}	1.19
3250	2.61×10^{-2}	0.84	-1.50×10^{-3}	1.16
3750	2.44×10^{-2}	0.72	-1.54×10^{-3}	1.14
4250	2.23×10^{-2}	0.66	-1.59×10^{-3}	1.12
4750	3.62×10^{-2}	0.96	-1.31×10^{-3}	1.22

R and q_r as a function of the resolved grid-scale means. Overall, good agreement is found between the radar-retrieved and model-predicted estimates of R over the 10-day analysis period centered around the TWP-ICE IOP, including both active and suppressed phases of the summer monsoon. Both the model and radar suggest a close relationship between $\sigma(R)$ and $\mu(R)$; other variables are found to be less strongly correlated with $\sigma(R)$. Because the ratio $\sigma/\mu(R)$ is found to be asymptotic and exhibits large variability for small $\mu(R)$, we simply parameterize $\sigma(R)$ as a function of $\mu(R)$ using both the model output and radar data.

Based on the overall good agreement between the area-averaged model output and radar data at a height of 2.5 km, the model output for the surface (at the model's inherent grid spacing) is used to formulate a scale-dependent power-law parameterization for $\sigma(R)$ as a function of $\mu(R)$ $[\sigma(R) = a\mu(R)^b]$ in which both a and b are linear functions of Δ (see section 3b). This formulation can be easily implemented in large-scale models to represent more accurately the subgrid-scale variability in R. Moreover, a relationship is also presented to relate $\mu(R)$ to the shape parameter of the rain-rate gamma distribution.

The confidence in the model output as based on a detailed comparison with radar observations allowed us to mine the model output further and explore the height dependence of the spatial variability in both R and q_r, which is important for understanding the rain rate at cloud base and predicting the formation of rain aloft, respectively. Characteristic features in the profiles of the fitted power-law coefficients were observed for both R and q_r. To be specific, we found that the spatial variability of q_r increased as one moved downward from the melting level, which we attributed to a combination of evaporation (i.e., smaller drops are preferentially evaporated, thus broadening the range of q_r), melting, and self-collection. Similar changes were identified for R except with a pronounced decrease in the spatial variability below approximately 1.5 km, which was attributed to a convergence toward a narrower range of terminal fall speeds. The resulting parameterizations were provided in the form of lookup tables.

TABLE 5. As in Table 4, but for R.

	$\sigma[R(z)] = a(z)\mu[R(z)]^{b(z)}$			
	$a(z) = m_1(z)\Delta + x_1(z)$ $[(\mathrm{mm\,h^{-1}})^{1-b}]$		$b(z) = m_2(z)\Delta + x_2(z)$ (unitless)	
z (m)	$m_1(z)$ $[(\mathrm{mm\,h^{-1}})^{1-b}\,\mathrm{km^{-1}}]$	$x_1(z)$ $[(\mathrm{mm\,h^{-1}})^{1-b}]$	$m_2(z)$ $(\mathrm{km^{-1}})$	$x_2(z)$ (unitless)
250	2.15×10^{-2}	0.54	-3.12×10^{-3}	1.32
750	2.22×10^{-2}	0.55	-3.01×10^{-3}	1.32
1250	2.34×10^{-2}	0.53	-3.42×10^{-3}	1.36
1750	2.29×10^{-2}	0.53	-2.88×10^{-3}	1.33
2250	2.23×10^{-2}	0.50	-2.73×10^{-3}	1.32
2750	2.20×10^{-2}	0.48	-2.50×10^{-3}	1.31
3250	2.17×10^{-2}	0.45	-2.02×10^{-3}	1.30
3750	2.13×10^{-2}	0.44	-1.58×10^{-3}	1.28
4250	2.08×10^{-2}	0.42	-1.04×10^{-3}	1.27
4750	2.00×10^{-2}	0.40	-3.12×10^{-4}	1.26

The primary motivation for this study is to parameterize the subgrid-scale variability R and q_r for use in large-scale models, although the results are likely also applicable to the field of satellite retrievals. For example, an accurate representation of the spatial heterogeneity of R within a given sensor field of view (i.e., beamfilling) has been recognized by the community as a major problem (e.g., Yang et al. 2006; Turk et al. 2008; Sapiano and Arkin 2009; Wolff and Fisher 2009). Moreover, Kirstetter et al. (2015) recently demonstrated that satellite-based precipitation radars are prone to errors that are inherently related to the assumed nonuniform beamfilling approach. The results presented herein provide a useful tool for constraining subpixel-scale variability in satellite-retrieved rain-rate and rainwater mixing ratio estimates, at least over the tropics.

Acknowledgments. Authors Z. Lebo and G. Feingold thank the U.S. Department of Energy's Atmospheric System Research Program under Grant 3RR1GSL; C. Williams and V. Larson gratefully acknowledge support by the Office of Science (BER) of the U.S. Department of Energy, under Grants DE-SC0008555 and DE-SC0008668, respectively. We also thank Drs. Peter May and Alain Protat of BoM for providing processed CPOL data for this analysis.

APPENDIX

Continental Convection Case

To investigate the robustness of the $\sigma(R)$–$\mu(R)$ relationships proposed in this work, an idealized simulation of a continental squall line is performed. The setup is nearly identical to that used in Lebo and Morrison (2014) and Lebo (2014). The only differences between those simulations and the one performed herein are that the microphysics model used here is the conventional Morrison et al. (2009) two-moment scheme (i.e., the same model used for the TWP-ICE simulations except that the droplet number concentration is fixed at 250 cm^{-3}) and that the horizontal and vertical resolutions are increased to 250 and 120 m, respectively. The case simulated herein has been simulated in other frameworks and has produced results that agree well with observations (Morrison et al. 2012). The final 4 h of the 8-h simulation is used for the following analysis.

Analogous to the results presented for the TWP-ICE simulations and observations, joint PDFs of $\sigma(R)$ and $\mu(R)$ are computed for different sampling footprints. Because of the smaller domain (at least in the y direction) used for the squall-line simulation, the 60-km sampling footprint is omitted. Fewer samples are used to

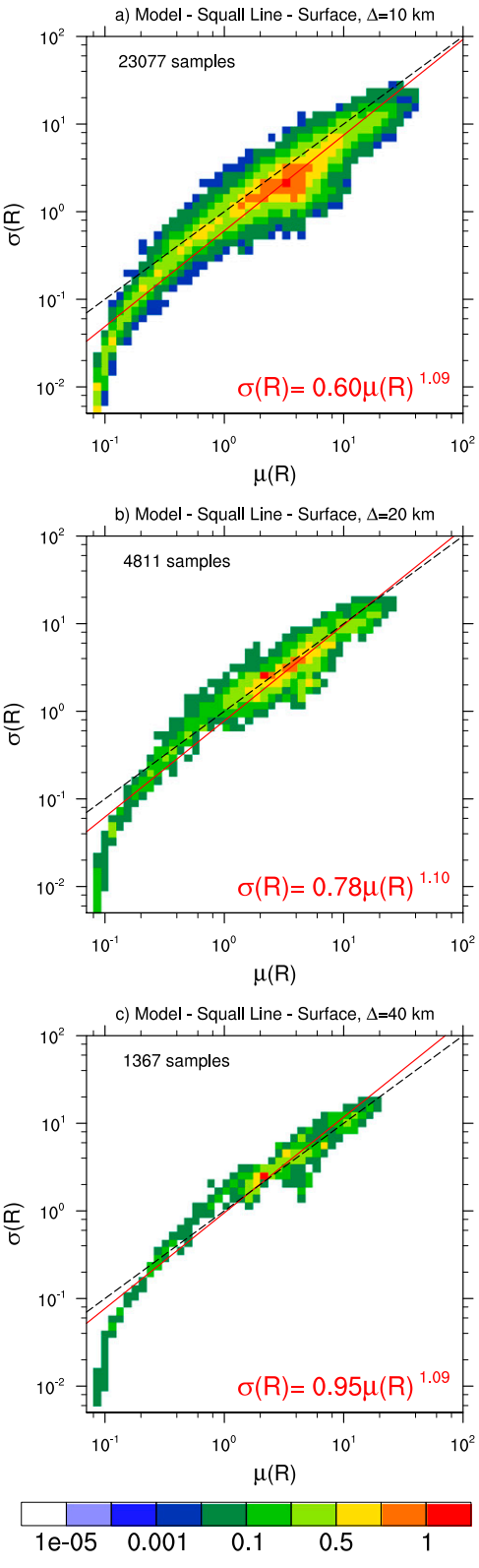

FIG. A1. As in Fig. 8, but for the idealized continental squall-line simulation.

construct each joint PDF than were used for the TWP-ICE results because the squall-line domain is smaller and the simulation is shorter (4 h of analysis vs 10 days). The joint PDFs for the continental squall-line simulation are more confined than those for the tropical convection simulations (cf. Fig. 8 with Fig. A1). This may be due to several factors, including the extent of organization in the simulated systems and the sampling size. Of interest is that the coefficients of the power-law fit are nearly identical to those computed for the TWP-ICE simulation and observations. The exponent is found to be slightly smaller for the squall-line simulation than for the tropical convection simulation, although the exponent corresponds well to that predicted based on the TWP-ICE observations. The similarities in the fits presented in Figs. 8 and A1 are remarkable given the substantial differences between the two simulations: different boundary conditions (periodic vs open in the line-normal direction and periodic in the line-parallel direction for the tropical convection and squall-line simulations, respectively), different forcings (the squall-line simulation is only forced for the first 1 h whereas the TWP-ICE simulation is forced throughout the simulation period), different resolutions (500 vs 250 m for the tropical convection and squall-line simulations, respectively), and different levels of organization (isolated, single-cell convection vs well-organized linear convection in the tropical convection and squall-line simulations, respectively).

Although these results cannot be used to definitively establish a universal relationship between $\sigma(R)$ and $\mu(R)$, the similarities are promising. Future endeavors that consider a broad array of cloud types are needed to determine either a universal relationship or a regime-dependent relationship between $\sigma(R)$ and $\mu(R)$.

REFERENCES

Boutle, I. A., S. J. Abel, P. G. Hill, and C. J. Morcrette, 2014: Spatial variability of liquid cloud and rain: Observations and microphysical effects. *Quart. J. Roy. Meteor. Soc.*, **140**, 583–594, doi:10.1002/qj.2140.

Bringi, V. N., C. R. Williams, M. Thurai, and P. T. May, 2009: Using dual-polarized radar and dual-frequency profiler for DSD characterization: A case study from Darwin, Australia. *J. Atmos. Oceanic Technol.*, **26**, 2107–2122, doi:10.1175/2009JTECHA1258.1.

Cheng, A., and K. Xu, 2009: A PDF-based microphysics parameterization for simulation of drizzling boundary layer clouds. *J. Atmos. Sci.*, **66**, 2317–2334, doi:10.1175/2009JAS2944.1.

Cho, H., K. P. Bowman, and G. R. North, 2004: A comparison of gamma and lognormal distributions for characterizing satellite rain rates from the Tropical Rainfall Measuring Mission. *J. Appl. Meteor.*, **43**, 1586–1597, doi:10.1175/JAM2165.1.

Dai, A., 2006: Precipitation characteristics in eighteen coupled climate models. *J. Climate*, **19**, 4605–4630, doi:10.1175/JCLI3884.1.

——, and K. E. Trenberth, 2004: The diurnal cycle and its depiction in the Community Climate System Model. *J. Climate*, **17**, 930–951, doi:10.1175/1520-0442(2004)017<0930:TDCAID>2.0.CO;2.

Fridlind, A., A. Ackerman, J. Petch, P. Field, A. Hill, G. McFarquhar, S. Xie, and M. Zhang, 2010: ARM/GCSS/SPARC TWP-ICE intercomparison study. NASA Tech. Memo. 215858, 24 pp. [Available online at http://permanent.access.gpo.gov/gpo3614/20100033502_2010034274.pdf.]

——, and Coauthors, 2012: A comparison of TWP-ICE observational data with cloud-resolving model results. *J. Geophys. Res.*, **117**, D05204, doi:10.1029/2011JD016595.

Golaz, J., V. E. Larson, and W. R. Cotton, 2002: A PDF-based model for boundary layer clouds. Part I: Method and model description. *J. Atmos. Sci.*, **59**, 3540–3551, doi:10.1175/1520-0469(2002)059<3540:APBMFB>2.0.CO;2.

Griffin, B. M., and V. E. Larson, 2013: Analytic upscaling of local microphysics parameterizations. Part II: Simulations. *Quart. J. Roy. Meteor. Soc.*, **139**, 58–69, doi:10.1002/qj.1966.

Haddad, Z. S., S. L. Durden, and E. Im, 1996: Parameterizing the raindrop size distribution. *J. Appl. Meteor.*, **35**, 3–13, doi:10.1175/1520-0450(1996)035<0003:PTRSD>2.0.CO;2.

Hubbert, L., and V. N. Bringi, 1995: An iterative filtering technique for the analysis of copolar differential phase and dual-frequency radar measurements. *J. Atmos. Oceanic Technol.*, **12**, 643–648, doi:10.1175/1520-0426(1995)012<0643:AIFTFT>2.0.CO;2.

IPCC, 2007: Summary for policymakers. *Climate Change 2007: The Physical Science Basis*, S. Solomon et al., Eds., Cambridge University Press, 1–18.

Keenan, T. D., K. Glasson, F. Cummings, T. S. Bird, J. Keeler, and J. Lutz, 1998: The BMRC/NCAR C-band polarimetric (CPOL) radar system. *J. Atmos. Oceanic Technol.*, **15**, 871–886, doi:10.1175/1520-0426(1998)015<0871:TBNCBP>2.0.CO;2.

Kirstetter, P., Y. Hong, J. J. Gourley, M. Schwaller, W. Petersen, and Q. Cao, 2015: Impact of sub-pixel rainfall variability on spaceborne precipitation estimation: Evaluating the TRMM 2A25 product. *Quart. J. Roy. Meteor. Soc.*, **141**, 953–966, doi:10.1002/qj.2416.

Kumar, V. V., C. Jakob, A. Protat, P. T. Pay, and L. Davies, 2013: The four cumulus cloud modes and their progression during rainfall events: A C-band polarimetric radar perspective. *J. Geophys. Res. Atmos.*, **118**, 8375–8389, doi:10.1002/jgrd.50640.

Larson, V. E., and J. Golaz, 2005: Using probability density functions to derive consistent closure relationships among higher-order moments. *Mon. Wea. Rev.*, **133**, 1023–1042, doi:10.1175/MWR2902.1.

——, and B. M. Griffin, 2013: Analytic upscaling of local microphysics parameterizations. Part I: Theory. *Quart. J. Roy. Meteor. Soc.*, **139**, 46–57, doi:10.1002/qj.1967.

——, D. P. Schanen, M. Wang, M. Ovchinnikov, and S. Ghan, 2012: PDF parameterization of boundary layer clouds in models with horizontal grid spacings from 2 to 16 km. *Mon. Wea. Rev.*, **140**, 285–306, doi:10.1175/MWR-D-10-05059.1.

Lebo, Z. J., 2014: The sensitivity of a numerically simulated idealized squall line to the vertical distribution of aerosols. *J. Atmos. Sci.*, **71**, 4581–4596, doi:10.1175/JAS-D-14-0068.1.

——, and H. Morrison, 2014: Dynamical effects of aerosol perturbations on simulated idealized squall lines. *Mon. Wea. Rev.*, **142**, 991–1009, doi:10.1175/MWR-D-13-00156.1.

May, P. T., and T. D. Keenan, 2005: Evaluation of microphysical retrievals from polarimetric radar with wind profiler data. *J. Appl. Meteor.*, **44**, 827–838, doi:10.1175/JAM2230.1.

Meneghini, R., and J. A. Jones, 1993: An approach to estimate the areal rain-rate distribution from spaceborne radar by the use of multiple thresholds. *J. Appl. Meteor.*, **32**, 386–398, doi:10.1175/1520-0450(1993)032<0386:AATETA>2.0.CO;2.

Morrison, H., G. Thompson, and V. Tatarskii, 2009: Impact of cloud microphysics on the development of trailing stratiform precipitation in a simulated squall line: Comparison of one- and two-moment schemes. *Mon. Wea. Rev.*, **137**, 991–1007, doi:10.1175/2008MWR2556.1.

——, S. A. Tessendorf, J. Ikeda, and G. Thompson, 2012: Sensitivity of a simulated midlatitude squall line to parameterization of raindrop breakup. *Mon. Wea. Rev.*, **140**, 2437–2460, doi:10.1175/MWR-D-11-00283.1.

Sapiano, M. R. P., and P. A. Arkin, 2009: An intercomparison and validation of high-resolution satellite precipitation estimates with 3-hourly gauge data. *J. Hydrometeor.*, **10**, 149–166, doi:10.1175/2008JHM1052.1.

Stephens, G. L., and Coauthors, 2010: Dreary state of precipitation in global models. *J. Geophys. Res.*, **115**, D24211, doi:10.1029/2010JD014532.

Turk, F. J., P. Arkin, E. E. Ebert, and M. R. P. Sapiano, 2008: Evaluating high-resolution precipitation products. *Bull. Amer. Meteor. Soc.*, **89**, 1911–1916, doi:10.1175/2008BAMS2652.1.

Weisman, M. L., W. C. Skamarock, and J. B. Klemp, 1997: The resolution dependence of explicitly modeled convective systems. *Mon. Wea. Rev.*, **125**, 527–548, doi:10.1175/1520-0493(1997)125<0527:TRDOEM>2.0.CO;2.

Wolff, D. B., and B. L. Fisher, 2009: Assessing the relative performance of microwave-based satellite rain-rate retrievals using TRMM ground validation data. *J. Appl. Meteor. Climatol.*, **48**, 1069–1099, doi:10.1175/2008JAMC2127.1.

Yang, S., W. S. Olson, J. J. Wang, T. L. Bell, E. A. Smith, and C. D. Kummerow, 2006: Precipitation and latent heating distributions from satellite passive microwave radiometry. Part II: Evaluation of estimates using independent data. *J. Appl. Meteor. Climatol.*, **45**, 721–739, doi:10.1175/JAM2370.1.